An efficient computational model for macroscale simulations of moving contact lines

Yi Sui, Peter D.M. Spelt

An efficient computational model for macroscale simulations of moving contact lines

Y. Sui[1,2] and Peter D. M. Spelt[3,4]

[1]*Department of Chemical Engineering, Imperial College London, London, SW7 2AZ, UK*
[2]*School of Engineering and Materials Science, Queen Mary University of London, London, E1 4NS, UK*
[3]*Département Mécanique, Université de Lyon 1, France*
[4]*Laboratoire de Mécanique des Fluides & d'Acoustique (LMFA), CNRS, Ecully, France*

Abstract

We propose an efficient level-set approach for numerical simulation of moving contact lines. The main purpose is to formulate and test a model wherein the macroscale flow is resolved while the effects of the microscopic region near a contact line are represented using asymptotic theories. The model covers viscous as well as inertial regimes. Test simulations include axisymmetric displacement flow in a tube and droplet spreading on a flat surface. The results show that the present approach leads to excellent convergence properties even with very coarse grids; furthermore, the results agree well with asymptotic analysis, with those obtained with a method for direct numerical simulations (wherein an adaptive grid is used) and also with experiments.

Keywords: moving contact line, macroscale simulation, level-set method, viscous regime, inertial regime, asymptotic theories

1. Introduction

Many phenomena in nature and industry involve multiphase flows with moving contact lines, including any form of droplet spreading/impact on a solid surface, coating flows and displacement flows (of oil with CO_2, for example). A major challenge in numerical simulations of moving contact lines is that the conventional hydrodynamic theory combined with a no-slip boundary condition leads to a non-integrable stress singularity at the contact line[1,2]. In order to alleviate this stress singularity, various approaches have

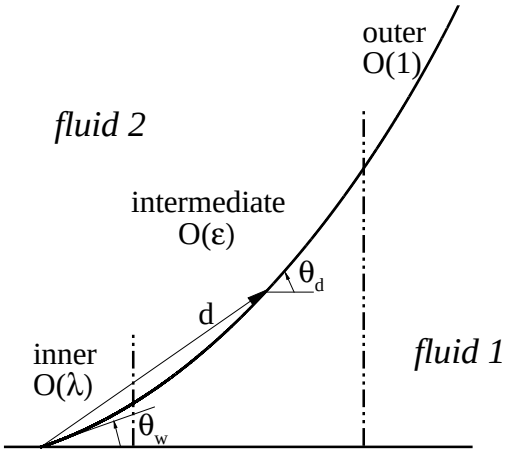

Figure 1: Three regions in the vicinity of a moving contact line; λ represents slip length, $\epsilon = 1/\mid \ln\lambda \mid$.

been proposed, such as assuming a precursor-film[3], or a diffuse-interface method[4,5], amongst others. One of the best documented methods is that wherein the no-slip condition is replaced by a slip condition, thereby introducing a slip length parameter (e.g., Ref[6]). Although the physical basis for slip remains unclear, and an integrable singularity in the pressure at the contact line usually remains (it can be avoided by using a different slip model if the contact angle is less than 90^o [7,8]), theoretical results of such an approach (e.g., Refs[9–13]) have been widely used and compare well with experiment[14,15]. The fact that the slip length must be taken to be much smaller than other length scales in a flow remains a major hurdle in numerical simulations of these flows (a similar problem arises in the other approaches mentioned above), however. In order to obtain mesh-convergent results, the slip length, which is usually inferred to be of nano-meter scale (e.g., Ref.[16]), must be resolved in direct numerical simulations with a slip-length-based method[17–21].

An efficient approach for large-scale simulations of flows with moving contact lines could be to only resolve the macroscopic scale far away and

modelling the microscopic region near the contact line on the basis of hydrodynamic theories (e.g.,[9–11,13]). With a slip boundary condition at the wall, such moving-contact-line theories have been well developed, such as that of Cox[9] for relatively slow contact-line motion. However, a computational method relying on the validity of asymptotic theories is expected to be applicable for flows solely within a part of parameter space. We shall use the following independent dimensionless groups: the capillary number (defined as $Ca_{cl} = \mu_1 U_{cl}/\sigma$, where μ is fluid viscosity, U_{cl} is the contact-line speed and σ represents surface tension) and the Reynolds number ($Re = \rho_1 U_{cl} L/\mu_1$ where ρ is the fluid density and L is a macroscopic length scale), along with the viscosity and density ratios of the two fluids involved, the slip length (made dimensionless with L) and the contact angle. Ca_{cl} and the dimensionless slip length are herein assumed small throughout. Also, further complications such as non-local hydrodynamic effects on the dynamic contact angle (as in curtain coating[26]) and rapid dewetting (for which asymptotic theory has not been well developed[21]) are not modelled here. However, the computational approach proposed here can be used as a framework to accommodate further theoretical advances, and to test other moving contact line models (such as Refs.[3,27]).

In the hydrodynamic theories for slow contact-line motion such as that of Cox[9], the interface is divided into three regions, with different length scales, as illustrated in Fig. 1. In the inner region, regardless of macroscopic geometry, a wedge flow pattern[1] is expected; the interface is almost planar and the angle it makes with the wall θ_w corresponds to the static advancing angle. Although in this theory a constant θ_w is assumed, there is evidence that the microscopic angle changes with the contact-line speed[27]. Such a dynamic contact angle is allowed in the numerical approach proposed here. In the intermediate region, the interfacial angle changes sharply due to viscous bending. In the outer region, classical hydrodynamic models with a no-slip boundary condition at the wall apply and the interface is affected by the large scale flow geometry. Cox' theory includes the interfacial angle in the vicinity of the contact line and relates the apparent angle θ_{app}, which can be obtained by extrapolating the interface profile from the outer region to the wall, to the microscopic contact angle θ_w and contact line speed U_{cl} by

$$g(\theta_{app}, r_v) = g(\theta_w, r_v) + Ca_{cl}\left(\ln\frac{L}{L_i}\right) + Ca_{cl}\left(Q_i - Q_o\right), \qquad (1)$$

where

$$g(\theta, r_v) = \int_0^{\theta} f(\beta, r_v) d\beta \tag{2}$$

and

$$f(\beta, r_v) = \frac{r_v(\beta^2 - \sin^2\beta)[(\pi - \beta) + \sin\beta\cos\beta] + [(\pi - \beta)^2 - \sin^2\beta](\beta - \sin\beta\cos\beta)}{2\sin\beta[{r_v}^2(\beta^2\sin^2\beta) + 2r_v[\beta(\pi - \beta) + \sin^2\beta] + [(\pi - \beta)^2 - \sin^2\beta]]}. \tag{3}$$

Here, $r_v = \mu_2/\mu_1$ is the viscosity ratio; L_i is a length scale characterizing the microscale region, which can be set as the slip length[21]; Q_i is a parameter depending on the inner slip model, r_v and θ_w; Q_o is also a parameter that is determined[9] by the geometry of the problem, r_v, θ_{app}, this is explained further in Sec.3 below.

Several approaches have been developed previously for large-scale simulations of flows with moving contact lines, based on the above theory. In these approaches, boundary conditions of the distance function (in a level-set method[22]) or volume fraction (in a VOF method[23]) have been developed to approximate the effect of the microscopic region near the contact line. In a level-set approach suggested by Spelt[18], the contact-line velocity is calculated from Eq. 1 and its location is obtained by integration. In another category of prior work, the effect of the contact-line region is modeled by imposing a contact angle[20,24] in a VOF method. These approaches can be theoretically supported by the conclusion of Kafka and Dussan[25] that the macroscopic dynamics is affected by the microscopic inner regime mainly through the interfacial angle in the intermediate region. In the work of Dupont and Legendre[24], the contact angle implemented is set to be a interfacial angle predicted by the theory of Ngan and Dussan[13], which is similar to that of Cox[9], at a length scale of 10 μm to the contact line, setting the inner length scale as 1 nm. Although grid convergence cannot be achieved in this way without using a slip boundary condition with the slip length resolved by the mesh resolution, it resulted in a favourable comparison with experimental results for droplet spreading. Using the asymptotic results of Cox[9], Afkhami et al.[20] proposed a mesh-dependent contact-angle boundary condition in the framework of a 2D VOF method and achieved good grid convergence. This is a very important merit since it forms the basis to simulate the moving contact line in a consistent manner. However, this model

has not as yet been compared with full-scale direct numerical simulations or experiments.

Furthermore, in prior work, as discussed above, asymptotic theory such as that of Cox[9] to order Ca_{cl}^0 has been employed, i.e., higher-order terms in e.g. Eq. 1 (i.e., Q_i and Q_o) have been neglected. This is mainly because these terms cannot be obtained analytically for general problems. Also, all available approaches are based on asymptotic theory for the creeping-flow regime, which are naturally limited to cases where inertial effects do not even enter the intermediate contact-line region. An approach that is valid for fast motion of a contact line is not yet available.

In the present study, a level-set approach for large scale simulations of moving contact line in both viscous and inertial regimes is formulated based on the theories of Cox[9] and Hocking and Rivers[11] for slow contact-line motion, and Cox[10] for cases involving rapid contact-line motion. With the present model, simulations including displacement flows in a tube and droplet spreading on a flat surface are carried out and the grid-convergence properties of the present model are tested. The model is validated by comparing the results with those from asymptotic analysis or full scale simulations with adaptive mesh refinement and the effect of previously neglected high-order terms is investigated. The present model is also validated against an experiment of fast droplet spreading.

2. Numerical Method

2.1. Level-set method

In the present model we assume both fluids to be incompressible, viscous and immiscible. The level-set approach employed here is based to some extent on that of Spelt[18], which is an extension of the method developed by Sussman et al.[22] to account for moving contact lines. We begin with briefly summarizing the level-set method before introducing the contact-line model.

The level-set function $\phi(\boldsymbol{x}, t)$ is taken to be a signed distance function from the interface, and the sign is used to distinguish between the two fluids; the zero level set corresponds to the interface. The level-set function follows the advection equation:

$$\frac{\partial \phi}{\partial t} + \boldsymbol{u} \cdot \nabla \phi = 0 \tag{4}$$

The advection equation only holds at the interface, and a 'redistance' step[28]

is used to ensure that ϕ at points away from the interface remains approximately the signed distance function.

The incompressible viscous fluids are governed by a single continuity equation and momentum equation valid throughout the computational domain,

$$\nabla \cdot \boldsymbol{u} = 0 \tag{5}$$

$$\rho[\frac{\partial \boldsymbol{u}}{\partial t} + \boldsymbol{u} \cdot \nabla \boldsymbol{u}] = -\nabla p + \frac{1}{\mathrm{Re}} \nabla \cdot [\mu(\nabla \boldsymbol{u} + \nabla \boldsymbol{u}^T)] + \boldsymbol{f}. \tag{6}$$

The local fluid density and viscosity are functions of ϕ, and they change smoothly across the interface over a length ξ that is proportional to the grid spacing:

$$\rho(\phi) = H(\phi) + (\rho_2/\rho_1)(1 - H(\phi)), \mu(\phi) = H(\phi) + (\mu_2/\mu_1)(1 - H(\phi)) \tag{7}$$

where H is the smoothed version of Heaviside function:

$$H(\phi) = \begin{cases} 0, & \phi < -\xi \\ \frac{1}{2}(1 + \phi/\xi + \sin(\pi\phi/\xi)/\pi), & \mid \phi \mid \leq \xi \\ 1, & \phi > \xi \end{cases} \tag{8}$$

ξ is set to be 1.5 times the grid spacing[18]. Surface tension is represented as a singular force density term $\boldsymbol{f}$ in the momentum equation, also smoothed out over a few mesh points:

$$\boldsymbol{f} = -\frac{1}{\mathrm{ReCa_{cl}}} \kappa(\phi) \nabla H(\phi) \tag{9}$$

where the interfacial curvature κ is calculated through:

$$\kappa(\phi) = \nabla \cdot \frac{\nabla \phi}{\mid \nabla \phi \mid}. \tag{10}$$

In the present implementation, a finite-volume method based on a uniform marker-and-cell (MAC) mesh is employed. The velocity components are defined at cell faces and scalar variables such as pressure and level-set function are defined at the cell centres. A fifth-order weighted essentially non-oscillatory (WENO) scheme[29] is employed in the discretization of the advection term in Eq. 4 using the local flow velocity as the up-winding direction. The continuity and momentum equations are coupled and solved with a standard projection method. More details can be found in Refs.[18,5].

2.2. Moving-contact-line models for slow and rapid contact-line motion

Kafka and Dussan[25] found that the macroscopic dynamics in the outer region is mainly affected by the microscopic inner regime near the contact line mainly through the interfacial angle in the intermediate region, which is of non-trivial size. It was found in Ref.[25] that for a nano-meter slip length, using an interfacial angle at a distance to the contact line ranging from $O(10nm)$ to $O(10\mu m)$ leads to almost the same results for the outer region (and consistent with the prediction resulting from resolving the inner region). This is a very important finding for macroscale simulations of moving contact lines, as it significantly increases the length scale that needs to be resolved in numerical simulation. The interfacial angle in the intermediate region can be predicted by asymptotic theories.

In Cox' viscous theory[9], the angle that the interface makes with the wall θ in the intermediate region follows from

$$g(\theta, r_v) = g(\theta_w, r_v) + Ca_{cl}\left(\ln\frac{d}{L_i}\right) + Ca_{cl}Q_i, \tag{11}$$

where d represents the distance to the contact line (illustrated in Fig. 1). As stated in Sec. 1, we account here for the higher-order term Q_i, investigate the dependencies of the result on the grid spacing and validate the model against asymptotic analysis and full scale simulations.

For cases wherein the contact line moves fast (small values of $Oh = \sqrt{Ca_{cl}/Re}$), Cox, in a later paper[10], further divided the intermediate region into a viscous intermediate sublayer where Eq. 11 applies and an inviscid intermediate layer, and matched these two sublayers in a transitional zone. The transition is at a distance from the contact line d^* chosen such that a Reynolds number, Re^*, based on the contact-line speed and d^* is of O(1). Cox[10] took this Reynolds number to be exactly unity, i.e., $d^* = Re^*/Re = 1/Re$. In recent work[21] for droplet spreading, Cox' inertial theory has been validated and modified. It was found that in order to achieve good agreement between the full scale simulation and the theory, a non-unity value should be used for Re^*, ranging from 0.2 to 1 (an average value of 0.37 was proposed). The interfacial angle, θ^* at the boundary of the intermediate viscous and inviscid sublayers ($d^* = Re^*/Re$) follows from

$$g(\theta^*, r_v) = g(\theta_w, r_v) + Ca_{cl}\left(\ln\frac{Re^*}{L_i Re}\right) + Ca_{cl}Q_i, \tag{12}$$

while in the inviscid subregion the interfacial angle can be obtained from

$$g_{iv}(\theta) - g_{iv}(\theta^*) - Ca_{cl}[h_{iv}(\theta) - h_{iv}(\theta^*)] = Ca_{cl}\ln(d\,Re/Re^*), \quad d^* < d < 1 \tag{13}$$

where

$$g_{iv}(\theta) = 1.53161\,(\theta - \sin\theta), \tag{14}$$

$$h_{iv}(\theta) = -2\ln(\sin\tfrac{1}{2}\theta) + 2\int_{\pi}^{\theta} \frac{\theta d\theta}{1-\cos\theta}. \tag{15}$$

Note, terms of $O(Ca_{cl}^{+1})$ have been left out by Cox[10] for simplicity, although these terms were included in the analysis of the viscous layer. Here we have re-instated these terms as we found in Ref.[21] that otherwise significant errors can occur.

In the present implementation of the level-set method, the level-set function is defined at cell centres, and the contact angle boundary condition is therefore implemented at a height of $0.5dz$ above the wall. We propose in the present model to determine the interfacial angle at this length scale from Eq.11 or Eq.13 in the case of slow or rapid contact-line motion, and to use the interfacial angle $\theta_{num} = \theta(z = 0.5dz)$ as the contact angle boundary condition. At $z = 0.5dz$, d can be approximated by $z \cdot \mathrm{cosec}[0.5(\theta_w + \theta)]$.

Contact angle hysteresis is not included in the present model, and θ_w is assumed to be the static advancing angle. Special attention should be paid to cases wherein the contact line moves fast: one needs to first check in which layer the interface at $z = 0.5dz$ lies and then decide to use Eq. 11 or 13, as appropriate; the determination of the value of constants such as Q_i is explained in Sec. 3 below. Details of the implementation of the contact-angle boundary condition in level-set methods are same as in Spelt[18] and are not repeated here.

If the grid is refined to such an extent that in fact the inner region is resolved after all, recourse should be taken to imposing just the microscale contact angle in conjunction with a slip condition, $U_w = \lambda(\partial u/\partial z)_w$. In what follows, we have simply kept the slip condition throughout. No artificially large slip coefficient is used.

The present model for slow contact-line motion differs from that of Dupont and Legendre[24] as follows. Although in both methods, an interfacial angle at a certain distance to the contact line is imposed, in the present model, θ_{num} depends on its distance to the contact line and thus is a function of mesh size, whereas this was taken to be independent of grid spacing ($d = 10\mu m$

in Eq. 11). A relatively large slip coefficient is not required and not used here. Also, terms corrected to Ca_{cl}^{+1} have been taken into account in the present model. The macroscale modelling along these lines for cases of rapid contact-line motion appears not to have been considered at all in prior work.

Finally, we note that no additional forcing at the contact line is imposed in this model, which at first sight may seem odd, since the wall stress components peak at the contact line. However, the peaks in wall shear stress and pressure are accounted for in the asymptotic analysis for the inner region, and the expressions in the above for the interfacial angle imposed at the first grid cell have been obtained theoretically through matching with the solution for the inner region. In other words, in the intermediate region, no additional forcing is to be imposed, neither in the full asymptotic theory nor in the present model. Conversely, should the shear stress or pressure distribution be required from a simulation wherein the present model is used, the pertinent theoretical results can be used (these are summarized in Ref.[21]).

2.3. Adaptive mesh refinement

In order to test the accuracy of the present model, we compare the results with full-scale direct numerical simulations with the slip length resolved. For full-scale simulation of flows with more or less realistic values of a dimensionless slip length, $\lambda = O(10^{-4})$, we have incorporated into our method in a previous study[21] the free open-source software package, PARAMESH[30], which is an adaptive mesh refinement (AMR) tool developed for parallel computing. It is categorized into the structured and block-based adaptive mesh refinement family. The computational domain is covered with a hierarchy of grid blocks having the identical logical structure. In the present method, the refining and coarsening of the grid blocks are based on whether the maximum distance of the grid block to the interface is smaller than a critical value. If true, a block is cut into two in all directions, respectively, producing four (in 3D this would be eight) children at a higher refinement level with the grid spacing in each direction is half that of its parent. As it is also required that the jump in refinement level between two adjacent blocks is not larger than 1, the mesh density varies relatively smoothly. Each block is surrounded by several layers of guard cells on each side, which protrude into the adjacent blocks. The connection between adjacent blocks and the implementation of boundary condition is realized by filling the guard cells with data from neighbouring blocks or user-defined boundary conditions, depending on the physical position of a block. In PARAMESH, all mesh blocks

have the same logic structure at all levels of refinement. Hence, once the flow solver is developed for one grid block, it can be easily applied to all other blocks independent of the level of refinement. In addition, the different blocks can be distributed relatively equally to different CPUs in an MPI parallel environment, which can support large-scale simulations. Various tests for droplet spreading have been carried out in Ref.[21] and shows the hybrid code, LS-PARAMESH, to be accurate and efficient in simulating multiphase flows with moving contact lines (although these are extensive computations despite the AMR, hence the need for the present model).

3. Results and discussion

Although from the work of Kafka and Dussan[25] discussed above, the present approach is expected to work for slow contact-line motion, it is unclear whether this extends to rapid contact-line motion. In order to test the validity of the present model for moving contact lines in both viscous and inertial regimes, simulations have been carried out for axisymmetric displacement flows in a tube and droplet spreading on a flat surface. The grid convergence properties of the present model are tested first; the simulation results are also compared with analytical solution, results from full-scale simulations using adaptive mesh refinement for flows with realistically small slip lengths, as well as an experiment for rapid droplet spreading. For all cases considered we have found that the global error in mass conservation for each phase to be below 0.5% throughout the simulations.

3.1. Viscous regime

We first test the present model by simulating steady axisymmetric displacement flows in a tube as defined in Fig. 2. One fluid, which is pumped into a tube with cross-sectional radius, a, displaces another fluid with which the tube is filled initially. The contact angle is defined from the displacing fluid. In the microscopic inner region, the contact angle θ_w is assumed to be the static advancing angle and set to be a constant. The viscosity and density ratios of the fluids, denoted by $r_v = \mu_2/\mu_1$ and $r_d = \rho_2/\rho_1$, are set to be 0.05. Gravity is not considered. The size of the computational domain is $a \times 8a$, which has been found long enough for the interface to develop into steady shapes. At the inlet ($z = 0$), fully-developed Poiseuille flow is imposed with a cross-sectionally averaged speed U. At the outlet, a zero normal velocity gradient outflow condition is used. At the centreline of the tube, a symmetry

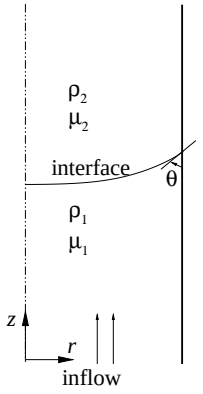

Figure 2: Illustration of axisymmetric displacement flow in a tube.

boundary condition is used and at the wall ($r = a$), the Navier slip boundary condition is employed. The tube radius a and the average flow velocity U (which is also the contact line speed when the interface has achieved a steady shape) are chosen as the macroscopic length and velocity scales, respectively. The Reynolds number is set to be unity as we found a further reduction of Re to lead to almost identical steady state interface profiles. The initial velocity condition in the tube is set as fully-developed Poiseuille flow. The initial interface profile is flat; this evolves into a deformed, but steady-state shape that we have found (in a previous study[34]) to be independent of the initial interface shapes used, for example when using as initial condition a steady wavy shape from a simulation conducted at another value of the Reynolds number. A dimensionless time step of 1.25×10^{-6} (normalized by a/U) has been used for all simulations of displacement flow; tests for the finest mesh have shown that halving the time step leads to visually identical steady shapes.

In the present study, although the contact angle in the inner region, θ_w is assumed to be the constant static advancing angle, the contact angle θ_{num} that is implemented as the boundary condition obviously depends on mesh size, contact line speed etc, according to Eq. 11, where the distance d to the contact line is determined as explained in Sec.2.2. Equation 11 can be

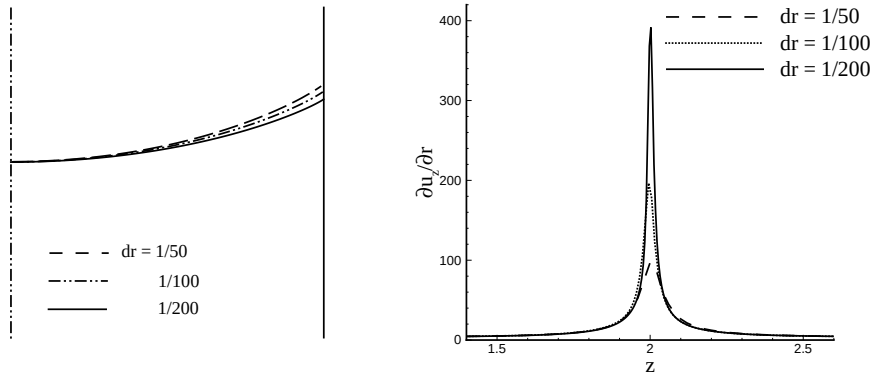

Figure 3: (a) Evidence that when just imposing the static angle for a realistically small slip length, results for the steady interface shapes obtained with an otherwise reasonable range of grid sizes appear not to converge. (b) Shear stress along the tube wall for different mesh resolutions. Parameter values are $Re = 1$, $Ca_{cl} = 0.01$, $\lambda = 10^{-6}$, and $\theta_{num} = 45^o$.

written alternatively as

$$g(\theta, r_v) = g(\theta_w, r_v) + Ca_{cl}\left(\ln\frac{d}{L_i\alpha}\right), \tag{16}$$

where $L_i = \lambda$ and the prefactor $\alpha = e^{-Q_i}$. Simulations are carried out to investigate the grid convergence properties of the present model. The cases considered are for $\theta_w = 45^o$ and $\lambda = 10^{-6}$ (normalized with a), corresponding to a realistic nanometer slip length if the tube radius is of the order of a millimeter. We use $\alpha = 10$ for this case, and this choice is discussed further below.

It is known that as long as the slip length is not resolved by the grid, convergence is not observed when using a constant contact angle θ_{num}, as confirmed in Fig. 3. It is seen that upon mesh refinement the steady interface profile becomes flatter. This can be easily understood from Eq. 16: if a constant contact angle θ_{num} is implemented, mesh refinement leads to reduction of the value of the second term on the right-hand side of Eq. 16, so that θ_w in the inner region simulated is in fact increasing which leads to interface shape that is flatter for the present parameters. In Fig. 3b the wall shear stress distribution is shown, it is seen that at the contact line the shear stress also does not appear to converge upon mesh refinement for the range of grid spacings used.

However, when using the present moving contact line model, the results

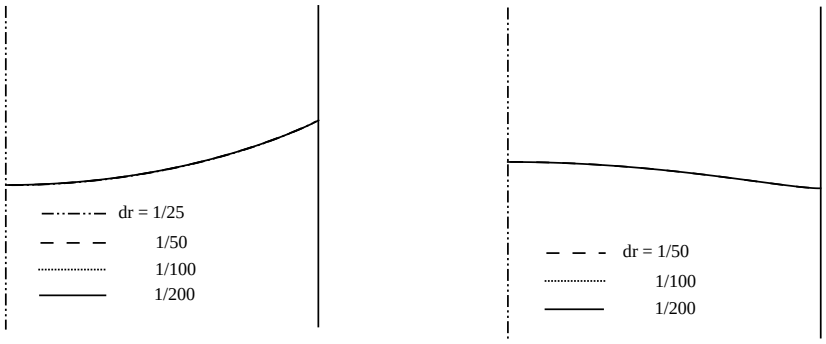

Figure 4: Steady interface shapes from the present numerical modeling with different grid sizes at $Re = 1$, $\lambda = 10^{-6}$ and Ca_{cl} =(a)0.01; (b)0.04.

are virtually independent of the grid spacing although the grid spacing (albeit varied over a significant range) is significantly larger than the slip length, as shown in Fig.4. The convergence of the method is further analyzed in Fig. 5(a). There, the relative error is defined as $[H(dr)-H(0.005)]/H(0.005)$, where $H(dr)$ is the difference in axial coordinate of the contact line and the interface location at the symmetry axis when using a grid spacing dr. The results appear to converge upon grid refinement. Furthermore, we plot in Fig. 5(b) $\theta^3_{num} - \theta^3_w$ versus the grid spacing. It is seen that it decreases logarithmically with the grid spacing, as expected. The grid convergence of the present model is a direct result of accurate prediction of interface profile (interfacial angle) in the intermediate region. According to the theoretical analysis of Kafka and Dussan[25], the outer interface profile is affected by the inner region mainly through the interfacial angle in the intermediate region, which depends on the distance to the contact line. Therefore, if the grid resolution lies within the intermediate region, which is not a stringent requirement, the present model is indeed expected to lead to consistent and accurate large-scale dynamics. However, because the microscopic inner region is far from being resolved, as stated above, it is of interest to investigate the behaviour of the wall shear stress near the contact line with mesh refinement, for which results are shown in Fig. 6. We find that the peak value of the wall shear stress is similar to that presented in Fig. 3b for the same

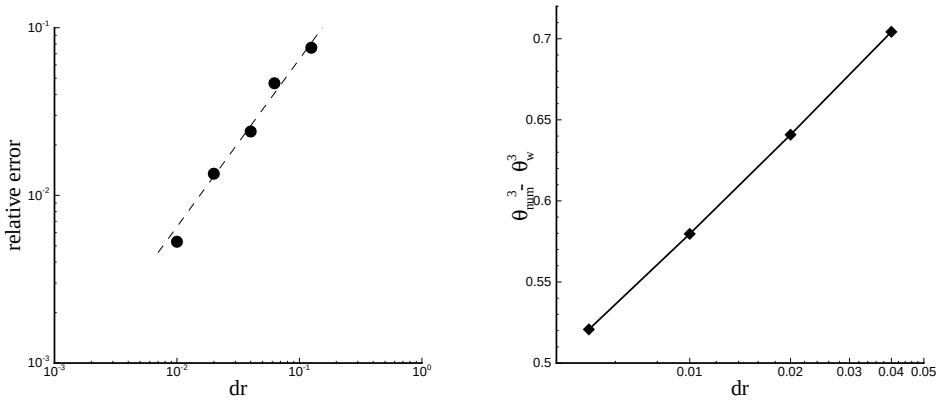

Figure 5: Convergence study for the case shown in Fig. 4(a). (a) Relative error in the interface height versus grid spacing, using the result for $dr = 0.005$ as the reference. (b) $\theta^3_{num} - \theta^3_w$ as a function of mesh size. In (a), the interface height is defined as the difference in the axial coordinate of the contact-line and of the interface at the symmetry axis, and the dashed line represents linear convergence.

mesh resolution. This is to be expected, as the flow is resolved within the intermediate region near the contact line, and upon refinement, more of this region is resolved, so when plotting the shear-stress along the wall, this gives the appearance of divergence; when the grid has been refined such that the first grid point is within the inner region, the method would switch in fact to a full DNS which does converge (see also Ref.[21] where this is established computationally for spreading droplets and good agreement is obtained with theory).

Of course, the present model is only expected to apply when Eq. 16 can accurately predict the interface shape in the intermediate region, that is for small Ca_{cl} and Re. Figure 7 presents the steady interface shapes from the present modeling for a large capillary number $Ca_{cl} = 0.1$, and it is seen that grid convergence is no longer achieved.

We have also compared results obtained from the present model with asymptotic analysis. A matched-asymptotic approach for creeping flows has been developed previously to predict the meniscus advancing or receding in a capillary tube[31]. The theoretical results have been found to agree very well with full scale direct numerical simulation[32–34] in the limit of small capillary number $Ca_{cl} < 0.07$ for an advancing contact line in the viscous

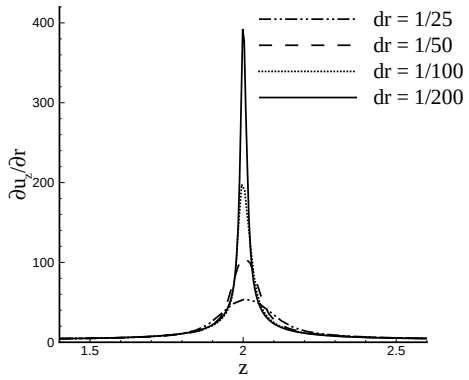

Figure 6: Shear stress along the tube wall for different mesh resolutions for Fig. 4a.

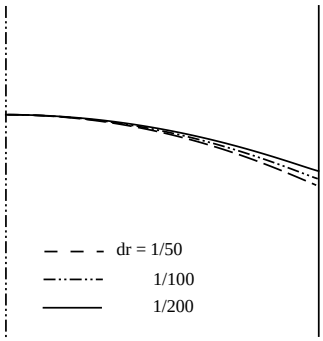

Figure 7: Steady interface shapes from numerical modeling with different grid sizes for $Re = 1$, $\theta_w = 45^o$, $\lambda = 10^{-6}$ and $Ca_{cl} = 0.1$.

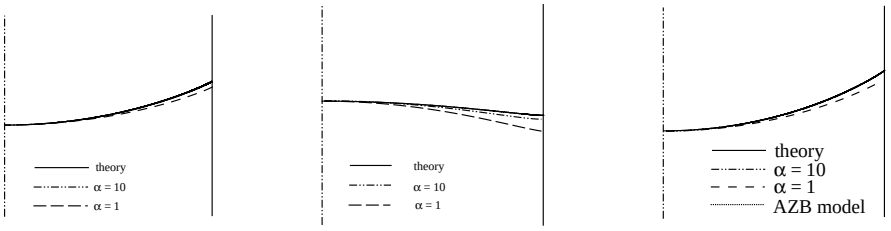

Figure 8: Steady interface shapes from numerical modeling with $dr = 0.01$ and theoretical model at $Re = 1$. (a) $\lambda = 10^{-6}$, $Ca_{cl} = 0.01$; (b)$\lambda = 10^{-6}$, $Ca_{cl} = 0.04$; (c)$\lambda = 10^{-4}$, $Ca_{cl} = 0.01$; the dot line represents the result obtained from the model of Afkhami et al.[20].

regime. Details of the theoretical model are not repeated here but can be found in pertinent literature[31,33]. It should be noted that for quantitative comparison, the prefactor α in Eq. 16 is required. For the displacement flow simulated here, α is a parameter that depends only on θ_w and the slip model[9]. Here we fit this prefactor by comparing our numerical results with that predicted by Ref.[33]. Since all present simulations have used a Navier slip boundary condition, there should be a single prefactor for a single value of θ_w. An example is shown in Fig. 8, where for $\theta_w = 45^o$ we find $\alpha = 10$ to give the best fit for all cases considered. With $\lambda = 10^{-6}$, we find very good agreement between the numerical modeling and asymptotic analysis can be achieved up to $Ca_{cl} = 0.05$; when $Ca_{cl} < 0.02$, there is almost no visible difference between the numerical and theoretical results, as can be seen from Fig. 8a. We have also carried out tests for $\alpha = 1$, that is neglecting Q_i in Eq. 11; it can be seen from Fig. 8a and b that this leads to quantitative deviations from the theoretical results. Similar results have also been found for various values of slip length in the present investigation, and one example is shown in Fig. 8c for $\lambda = 1 \times 10^{-4}$. It is seen that the agreement between the theory and the numerical simulation is excellent with $\alpha = 10$.

As reviewed in the Introduction, Afkhami et al.[20] developed a related macroscopic contact line model for the viscous regime, by drawing an analogy to Cox's viscous theory, albeit neglecting corrections to order Ca^{+1}. In their model the contact angle boundary condition at $z = 0.5dz$ is calculated from

$$g(\theta_{num}) = g(\theta_{apparent}) + Ca_{cl}\left(\ln\frac{0.5dz}{L}\right), \tag{17}$$

In their numerical tests, a constant apparent contact angle is prescribed and grid convergence was achieved. In principle, θ_{app} can be obtained from various empirical correlations[20] and this is tested in the present study, using the Hoffman-Voinov-Tanner law, $\theta^3_{apparent} = \theta^3_w + 9Ca_{cl}\left(\ln\frac{L}{\lambda}\right)$. The result is presented in Fig. 8c for $Ca = 0.01$ and $\lambda = 10^{-4}$, it is seen that the steady interface profile closely resembles those obtained from the present model with $\alpha = 1$ and deviates from the theoretical prediction presumably due to the neglected high-order terms of Cox's theory.

The second test of the present model is for axisymmetric slow spreading of a droplet, with diameter D, on a flat surface. The initial shape of the drop is chosen to be a circular cap with constant contact angle θ_{ini}, and a smaller microscopic contact angle θ_w is prescribed so that a high-curvature region is formed at the contact line that initiates the spreading of the droplet towards a shape corresponding to θ_w. The simulations will be identified in terms of an Ohnesorge number, which indicates the effect of inertia. Other parameters includes $\lambda = 10^{-4}$ (normalized by D) and $r_d = r_v = 0.1$. In the present numerical modeling, the instantaneous contact angle θ_{num} is calculated from Eq. 11. For droplet spreading with negligible density and viscosity ratios, Q_i is available and can be found in[11] (The present Q_i equals the value of Q_1 in Ref.[11] plus one); in the present test case, $\theta_w = 30^o$, which gives $Q_i = -0.7$. The results from the present model are compared with full-scale simulation with adaptive mesh refinement (the latter have been tested elsewhere[21]). In the full-scale simulation, the computation domain is of unity dimensions and doubling the domain size leads to nearly identical results; the finest mesh resolution is $dr = 1/5120$, which is sufficient to give mesh-convergent results[21]. A time-step convergence study has been carried out and the dimensionless time steps (normalized by $\rho R^2/\mu$) employed are 10^{-5} and 5×10^{-6} for mesh resolutions $dr = 1/32, 1/64$ and $dr = 1/128, 1/256$ respectively.

In Fig. 9 results are presented for the temporal evolution of the contact line radius and speed. From Fig. 9a, the results represented by red lines, it is of course clear that when the grid spacing is significantly larger than the slip length, simulations with the contact angle θ_{num} set as the inner wetting angle cannot yield converged results; the drop spreads much faster than that from full scale fine mesh simulation with adaptive mesh refinement (DNS). With the present model, it is seen (black and blue lines) that virtual grid independency is achieved even with a very coarse mesh. Furthermore, the modeling results using Eq. 11 (Q_i is obtained from[11]) with $dr = 1/32$ can compare well to those of the DNS with $dr = 1/5120$. We also find

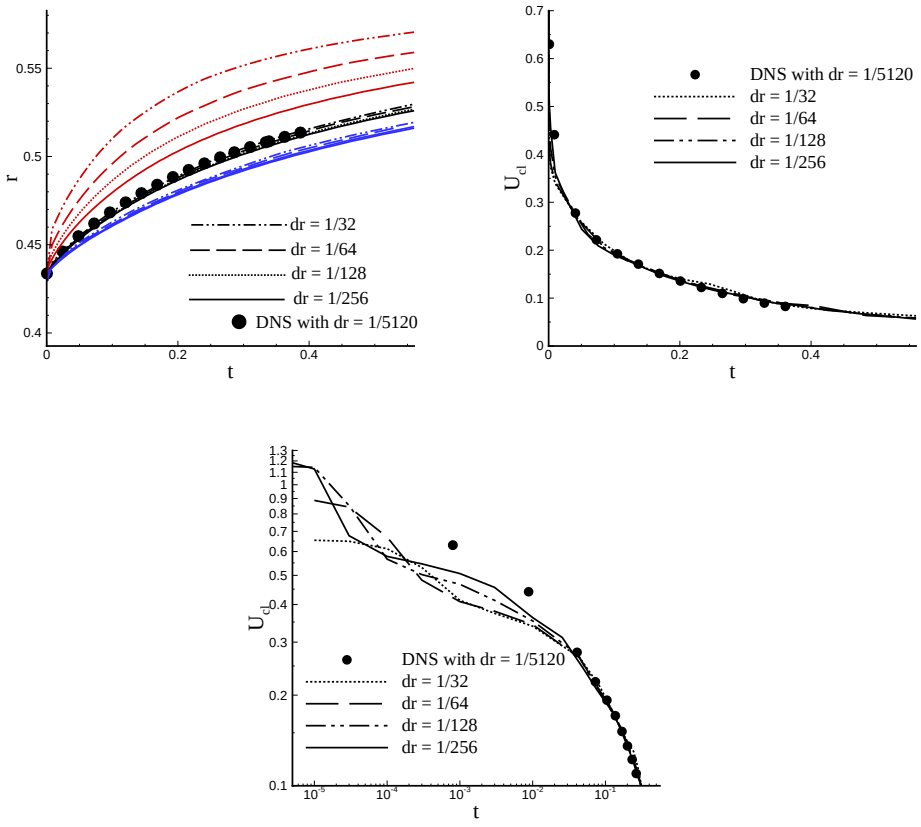

Figure 9: Axisymmetric droplet spreading with $r_v = r_d = 0.1$, $\lambda = 0.0001$, $\theta_w = 30^o$ and $Oh = 0.1$. (a) Contact line radius as a function of time. Red lines are for constant $\theta_{num} = 30^o$. Black lines are for θ_{num} inferred from Eq. 11. Blue lines are for θ_{num} from Eq. 11 with Q_i neglected. Black dots are for direct numerical simulation with adaptive mesh refinement. (b) Contact line speed as a function of time. Black lines are for θ_{num} inferred from Eq.11. Black dots are for full scale simulation with adaptive mesh refinement. (c) Replot of (b) with both axes on logarithmic scales.

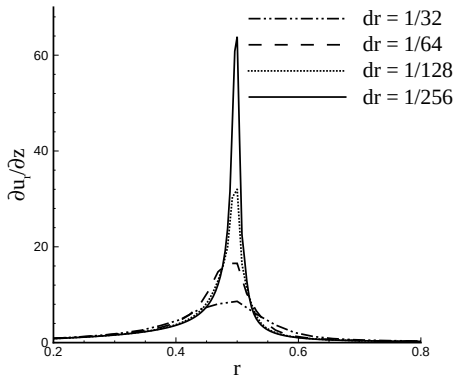

Figure 10: Wall shear stress profiles obtained with different mesh resolutions at $t = 0.32$.

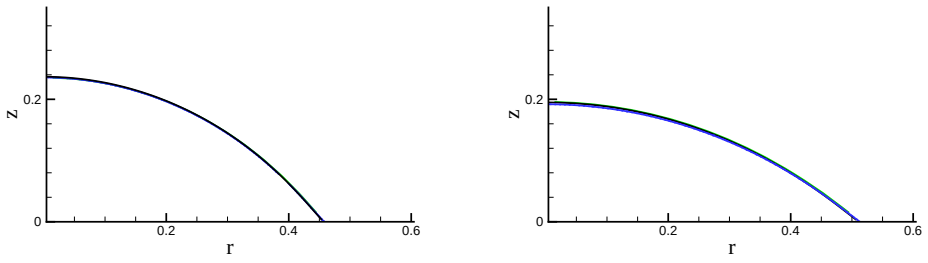

Figure 11: Instantaneous interface profiles from numerical modeling with $dr = 1/32$ green line $dr = 1/128$ (black line) and full scale simulation with $dr = 1/5120$ (blue line). t =(a) 0.064;(b)0.384

Grid spacing	Wetted distance	Relative error
1/32	0.0808	0.043
1/64	0.0794	0.025
1/128	0.0782	0.009
1/256	0.0775	

Table 1: Convergence study of the distance travelled by the contact line corresponding to Fig. 11(b). The relative error is defined as the difference with the most accurate result with $dr = 1/256$.

that neglecting the term Q_i, as has been done in previous work, leads to a quantitative difference and worsens the comparison with DNS. Figure 9b presents the mesh dependency study of the contact line speed as a function of time from the present modeling with taking into account the value of Q_i, and it is seen that the results are very close to the DNS data. In the present simulation, an initial downward velocity is applied which helps to trigger an initial spreading speed that may depend somewhat on the mesh resolution, as the asymptotic contact-line region resulting from this initial condition is very small. To investigate this in detail, a log-log plot of the contact line speed as a function of time is included in Fig. 9c to single out the very earliest data. We conclude from the figure that the results converge at shorter and shorter times towards the DNS data upon grid refinement i.e., the curves fold towards the DNS from later to shorter times. Figure 10 shows the wall shear stress for different mesh resolutions at $t = 0.32$. The behaviour is similar to that observed in Fig. 6 for the flow in a tube; as discussed there, the fact that upon grid refinement more of the intermediate region is resolved gives the appearance of divergence.

The instantaneous drop shapes obtained are presented in Fig.11, it is seen that results obtained with the model at different grid spacings - including a very coarse grid - are all very close. The small differences are analyzed further in Table 1 for Fig.11(b), where the results appear to converge. Furthermore, in Fig.11, the results obtained with the present model are seen to be also very close to the corresponding DNS results. An exact convergence to the DNS cannot result, as the model used is itself not exact (this has been investigated further in Ref.[21] using DNS) but the differences are very small.

Regarding the computational effort involved, a simulation using the present approach with $dr = 1/32$ takes about 5 minutes on a single PC, while a DNS

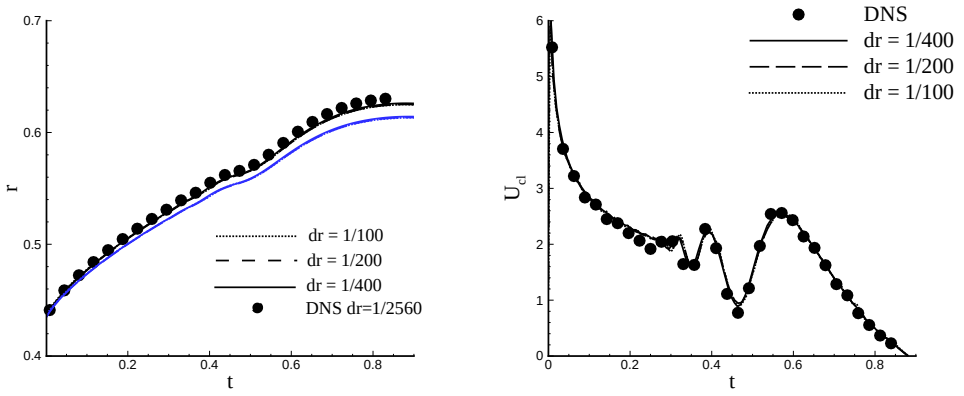

Figure 12: Axisymmetric droplet spreading with $r_v = r_d = 0.1$, $\lambda = 0.0001$,$\theta_w = 30^o$ and $Oh = 0.00316$. (a) Contact line radius as a function of time. θ_{num} is inferred from Eq. 11 or 13. Black lines are for Q_i from[11] and $Re^* = 0.37$. Blue lines are for neglected Q_i, h_{iv} terms and $Re^* = 1$. Black dots are for direct numerical simulation with adaptive mesh refinement. (b) Contact line speed as a function of time. Black lines are for the same case as in (a). Black dots are from DNS with adaptive mesh refinement.

simulation with a grid spacing of $dr = 1/5120$ takes 140,000 cpu hours on the High-Performance Computing facility at Imperial College London, typically using 64 processors.

3.2. Inertial regime

We now go beyond the slow-spreading regime. We first consider axisymmetrical rapid droplet spreading on a flat surface with parameters similar to that in the previous section except that the value of Oh is now reduced to 0.00316, to introduce strong inertial effects. From the results presented in Fig. 12, it can be seen that similar to the viscous model, the present inertial model also leads to results for contact-line radius and speed obtained with different grids to virtually overlap. The dimensionless time steps normalized by an inertial/capillary time scale $\sqrt{\rho R^3/\sigma}$ employed are 5×10^{-5} for simulations with the present model. With the present model, even using a very coarse mesh gives results that agree quite well with the DNS results (we have tested and found $dr = 1/2560$ leads to converged results for this case), when accounting for the appropriate value of Q_i. The value of Re^* is taken from previous work[21] and set to be 0.37. The results obtained when neglecting

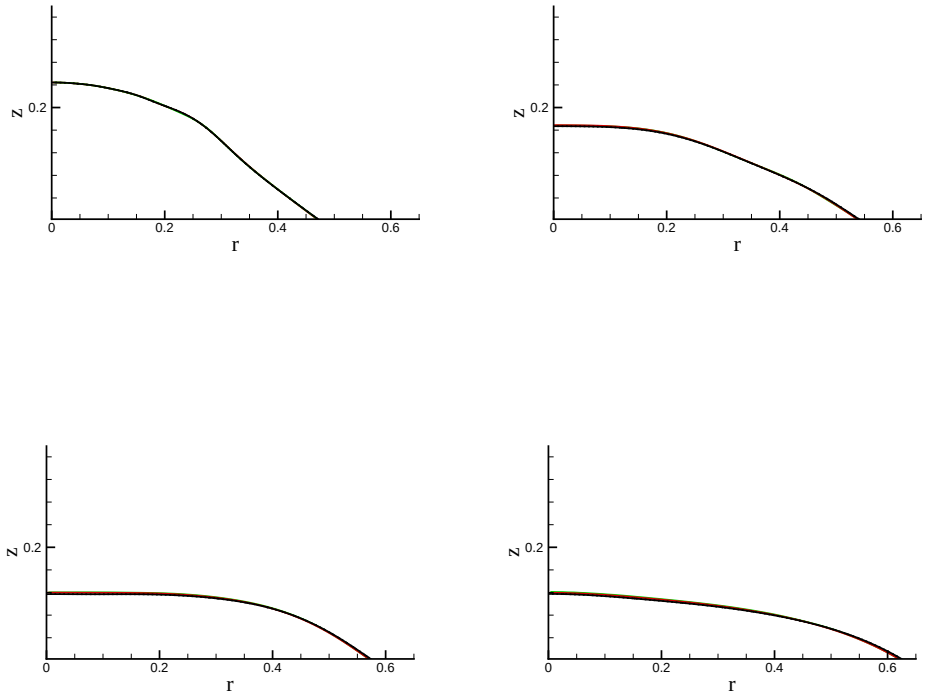

Figure 13: Instantaneous interface profiles from numerical modeling with $dr = 1/100$ green line $dr = 1/400$ (red line) and full scale simulation with $dr = 1/2560$ (black line). $t =$ (a)0.09; (b)0.36; (c)0.54; (d)0.8.

terms corrected to $O(Ca_{cl}^{+1})$ and $Re^* = 1$ deviate more from the direct numerical simulation. From Fig.13, where the grid-converged instantaneous drop shape compares well with that of DNS, it is seen that macro-scale dynamics like capillary waves traveling along the drop interface can be accurately captured with the present inertial model.

We further test the present inertial model by comparison with a recent experiment of rapid droplet spreading[35] where a novel mode of droplet pinch off following the deposition of a liquid droplet on a substrate has been identified. To facilitate this, we need to set a proper value of the slip length in the numerical model. In the present study, the slip length is inferred by fitting Cox's inertial theory[10] to the experimental data, as shown in Fig.14. In[10], the intermediate region is further divided into a viscous sublayer connected by a inviscid layer. At the outer edge of the viscous sublayer, the interfacial angle can be obtained with Eq. 12. The apparent angle then follows from

$$g_{iv}(\theta_{app}) - g_{iv}(\theta^*) - Ca_{cl}[h_{iv}(\theta_{app}) - h_{iv}(\theta^*)] = Ca_{cl}\ln(d_m Re/Re^*). \quad (18)$$

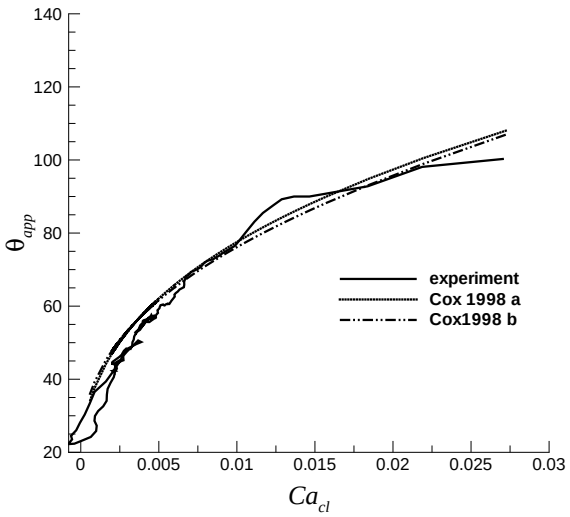

Figure 14: Apparent angle as a function of instantaneous Ca_{cl}. The experiment (from Ref.[35]) is for a water drop of $0.77mm$ in diameter with an small impact speed of $0.079m/s$ ($Oh = 0.006$ and $We = 0.033$) and $\theta_w = 23°$. The theoretical predictions are obtained from Eq. 12 and 18. Cox 1998a is for $\lambda = 10^{-16}m$ and a constant $\theta_w = 23°$, Cox 1998b is for $\lambda = 1$nm and a velocity-dependent contact angle.

In Ref.[10], d_m is of order 1; in recent work by the present authors[21], it was found that using $d_m = 0.2$ always leads to good agreement in apparent angle between the theory and full-scale simulation. Here we have used the value of 0.2. We find that in order to achieve good agreement with the experiment, an unrealistically small slip length needs to be employed. The physical explanation is investigated elsewhere[21]: it may be because the wetting angle in the microscopic inner region θ_w in the experiment is a function of the spreading rate. However, we have found using the inferred slip length with a constant θ_w to have the same effect on the apparent angle. We revisit this issue further below.

We have carried out simulations using the present model with the inferred slip length, and the parameter values set as in the experiment. The dimensions of the computational domain are twice the drop diameter in both directions, which is found to be large enough to neglect the boundary effect. The density ratio is set to be $r_d = 0.001$ and viscosity ratio $r_v = 0.05$, a further reduction of viscosity ratio leads to identical results. The dimensionless time step used is 2.5×10^{-5}. First tested is the mesh-dependency performance of the present model and the results are presented in Fig. 15. The results of the simulations obtained with the present model using different grid spacings

nearly coincide, for the instantaneous contact line radius as well as for the contact-line speed, even though the grid spacing is varied significantly and is much larger than the slip length.

In Cox's inertial theory for spreading, the intermediate region is divided into a viscous sublayer connected by an inviscid layer, and the transition is at $d^* = Re^*/Re$. In the viscous sublayer, the interface shape is identical to that in Cox's viscous theory. In the simulation of droplet spreading presented in the above, the value of Re decreases as the spreading rate decreases and hence d^* increases (i.e., the viscous sublayer becomes thicker). Therefore, at a late stage in the spreading process the location $z = 0.5dr$ ceases to be in the inviscid intermediate sublayer but lies in the viscous intermediate sublayer instead (e.g., for $dr = 1/100$, this occurs in the present case when $U_{cl} = 1.3$ and $Re = 39$). From this point onwards, θ_{num} is calculated from Eq. 11, which is in fact identical to Cox's viscous theory and thus leads to results for different grids in Fig. 15 to virtually overlap also at this stage.

In Fig. 15b, the second oscillation (after $t = 2$) coincides with the arrival of the capillary wave caused by a droplet ejection. At this instance in the experiment, the contact line overshoots and then recedes rapidly. In dewetting that is sufficiently rapid, the model of Cox[10] is not expected to perform well[21] and in fact ultimately leads to negative values of θ_{num}, so we have terminated the simulations when this point was reached in Fig. 15b due to current limitations of the asymptotic modelling.

In our previous work[21], for a realistic slip length $\lambda = 1nm$, we found that in order to achieve good agreement between the inertial theory of Cox and the experiment, a contact-line-speed-dependent contact angle, θ_{dyn}, must be used. Following a formula proposed by Sheng and Zhou[36], $\cos\theta_w = \cos\theta_{dyn} + B \cdot Ca_{cl}^n$, it was found $B = 9.6$ and $n = 0.64$ leads to excellent agreement, as shown in Fig. 14. We have carried out a simulation wherein this dynamic microscale contact angle is used with $\lambda = 1nm$ and the result is shown in Fig. 15a for the instantaneous contact line radius. It is seen that the result is almost identical to that obtained for a constant contact angle and an inferred, though unrealistically small, slip length, which confirms these two approaches have the same effect on the macroscale simulation; in the following, we adopt the static model as outlined above. Note, the static and dynamic models in Fig. 15 refer to the contact angle θ_w in the microscopic inner region, not to the contact angle boundary condition θ_{num} implemented at $z = 0.5dz$. The models of the latter affect the droplet evolution significantly, as discussed further below.

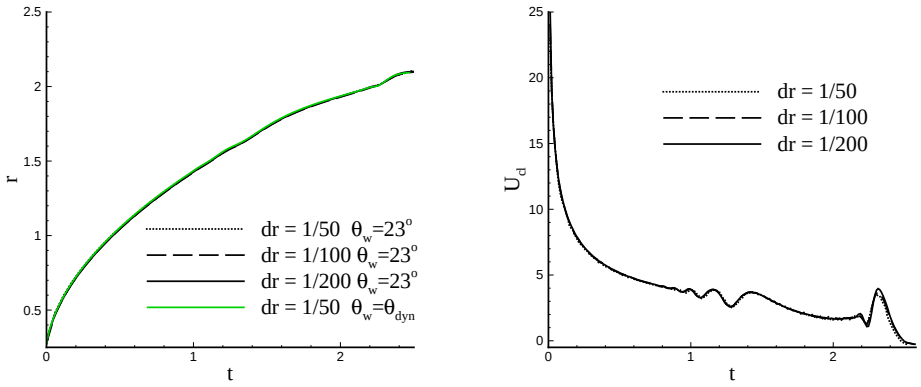

Figure 15: Axisymmetric droplet spreading on a flat surface with $Oh = 0.006$, $\theta_w = 23°$. (a) Contact line radius and (b) drop spreading speed as a function of time. In (a) the green line is for simulation using a dynamic microscopic contact angle instead of a constant θ_w as explained in the text.

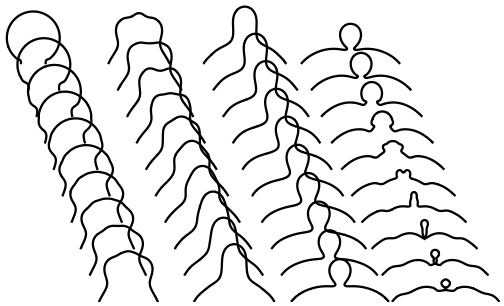

Figure 16: Instantaneous interface profiles from numerical model with time running from top to bottom, and then from left to right. $dr = 1/100$ and other parameters are the same as those in Fig. 15. $Q_i = -0.99$[11] and $Re^* = 0.37$.

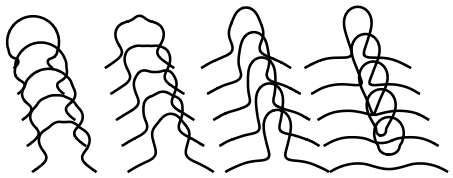

Figure 17: Instantaneous interface profiles from numerical model using a fixed contact angle $\theta_{num} = 23^o$ with time running from top to bottom, and then from left to right; $dr = 1/100$, and other parameters are the same as those in Fig. 15

.

Figure 16 presents the interface shapes during droplet spreading. Capillary waves are observed, leading to the formation of a narrow neck in the upper part of the droplet with its size decreasing with time (from the third column in the figure onwards). However, the neck size does not directly go to zero to result in pinch off (termed as first-stage pinch off in [35]); from the fourth column in Fig 16, it is seen that the neck re-expands (in the r direction) to a certain extent and after that a similar necking process happens again and finally leads to the ejection of a small droplet, which is termed second-stage pinch-off. The present simulation agrees very well with the experiment of Fig. 14, where a similar second-stage pinch off has been observed.

We have also carried out a simulation for $\theta_{num} = \theta_w = 23^o$, instead of calculating θ_{num} from Eq. 11 or 13. Other parameters are the same as in Fig. 16. The instantaneous droplet shapes are presented in Fig. 17. It is seen that a first-stage pinch-off is obtained, qualitatively different from experimental observation.

Quantitative comparisons have also been conducted. Figure 18a and b present the time evolution of the apparent angle and the capillary number based on spreading rate, respectively. According to Cox [9,10], the apparent angle is obtained by extending the interface from the outer region to the wall and finding the intersection angle, as illustrated in Fig. 19, where θ represents the interfacial angle and s is the interfacial distance to the contact line. A similar approach has also been adopted in the experiment [35]. From

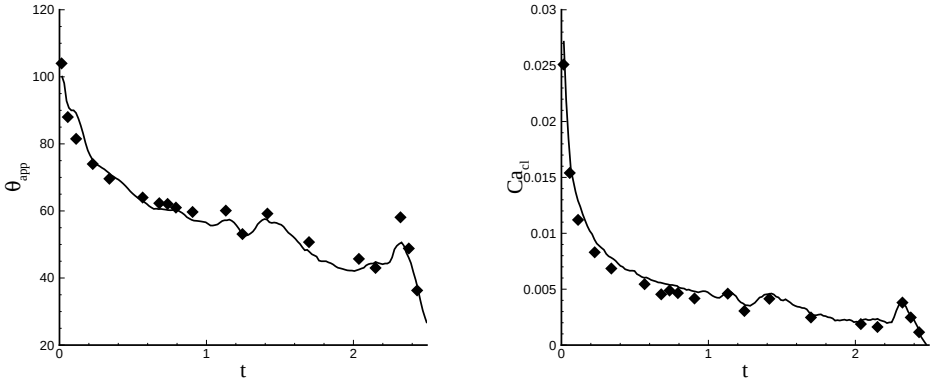

Figure 18: Temporal evolution of (a) apparent angle; (b) capillary number based on droplet spreading rate for the experiment (curves) and the numerical modeling (diamonds). Parameters are the same as those in Fig. 14.

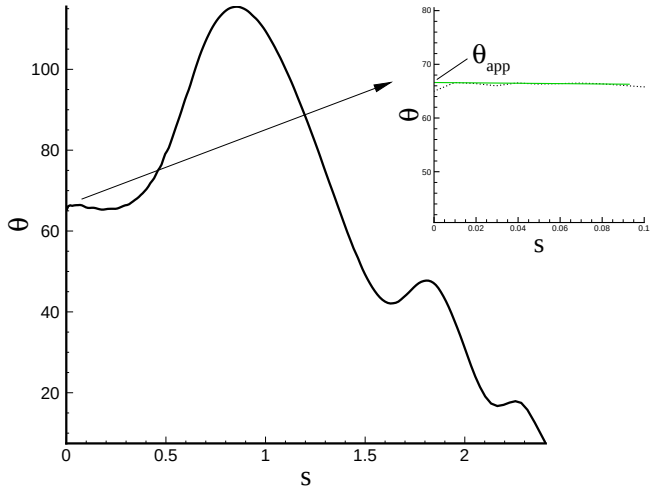

Figure 19: Illustration of the measurement of the apparent angle in numerical simulation.

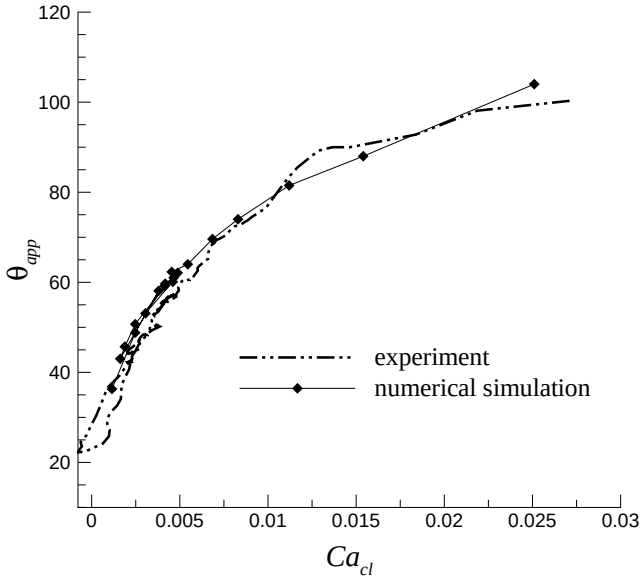

Figure 20: Apparent angle as a function of instantaneous capillary number for experiment and numerical modeling. Parameters are the same as those in Fig. 14.

Fig. 18, it is seen that good quantitative agreement is achieved. Hence the present inertial model with an inferred slip length can accurately predict the instantaneous contact line speed and the transient large scale dynamics.

We also compare the apparent angle as a function of capillary number and get reasonably good agreement, as shown in Fig. 20. Flat loops are observed in the experimental data, which are investigated in detail in Ref.[35]. From Fig. 20, it is seen that these flat loops have been captured by the numerical simulation using the present inertial model.

In summary, the required input beyond the standard ones for two-phase flows without contact lines are: the microscale contact angle and the slip length. However, the parameters Q_i in Eq. 12 and Re^* in Eq. 13 depend, in principle, on the geometry of the flow (this was already recognized by Cox[9]), so the values for these used herein are for the systems we have tested the model for. Even so, we are encouraged by the fact that Q_i in the tests for capillary rise in a tube are of the same order as in slow axisymmetric spreading. We envisage that in practice, the model proposed here could be used in various ways, depending on the amount of information available in any application. The minimum scenario would be to provide an estimated value for slip length and microscale angle, and using Q_i, Re^* to be of order unity. Next, recognizing not only that the values for Q_i and Re^* may be a bit different in another application, but the appropriate slip length value could be affected by the properties of the surface and the microscale angle

may pose a further uncertainty, it would be sensible to test the sensitivity of the results to the values used for these parameters. Of these, we would expect the microscale contact angle to be the dominant one.

4. Conclusion

Within the framework of the level-set method, we have developed an approach for macroscale simulation of multiphase flows with moving contact lines. Instead of resolving the microscopic region near the contact line directly, the present approach models its effect, mainly an interfacial angle, by using asymptotic theory[9,10], so that using the present model can capture the large-scale dynamics at much reduced computational cost. The present model has been tested by simulations including displacement flow in a tube, as well as slow and rapid droplet spreading on a flat surface. The results show that the present approach, in both viscous and inertial regimes, leads to grid-converged results even when using a very coarse mesh. Furthermore, the results from the present model agree quantitatively with asymptotic analysis, full-scale DNS results and also with experiments. These tests suggest the present model to be accurate and efficient for macroscale simulations of moving contact lines.

Financial support from EPSRC (Grant EP/E046029/1) is acknowledged.

[1] C. Huh, L.E. Scriven, Hydrodynamic model of steady movement of a solid/liquid/fluid contact line, Journal of Colloid and Interface Science 35 (1971) 85101.

[2] E. B. Dussan V., S. H. Davis, On the motion of a fluid-fluid interface along a solid surface, J. Fluid Mech. 65 (1974) 71-95.

[3] P. G. de Gennes, Wetting: statics and dynamics, Rev. Mod. Phys. 57 (1985) 827-863.

[4] D. Jacqmin, Contact-line dynamics of a diffuse fluid interface, Journal of Fluid Mechanics 402 (2000) 57-88.

[5] H. Ding, P. D. M. Spelt, C. Shu, Diffuse interface mode for incompressible two-phase flows with large density ratios, J. Comput. Phys. 226 (2007) 2078 -2095.

[6] E. B. Dussan V., On the speading of liquids on solid surfaces: static and dynamic contact lines. Annu. Rev. Fluid Mech. 11 (1979) 371-400.

[7] E. Ruckenstein, C. S. Dunn, Slip velocity during wetting of solids, J. Colloid Interface Sci. 59 (1977) 135138.

[8] D. N. Sibley, N. Savva, S. Kalliadasis, Slip or no slip? A methodical examination of the interface formation model using two-dimensional droplet spreading on a horizontal planar substrate as a prototype system., Phys. Fluids 24 (2012) 082105.

[9] R. G. Cox, The dynamics of the spreading of liquids on a solid surface. Part 1. Viscous flow, J. Fluid Mech. 168 (1986) 169-194.

[10] R. G. Cox, Inertial and viscous effects on dynamic contact angles, J. Fluid Mech. 357 (1998) 249-278.

[11] L. M. Hocking, A. D. Rivers, The spreading of a drop by capillary action, J. Fluid Mech. 121 (1982) 425–442.

[12] O.V. Voinov, Hydrodynamics of wetting, Fluid Dynamics 11 (1976) 714721.

[13] C. G. Ngan, E. B. Dussan V., On the dynamics of liquid spreading on solid surfaces, J. Fluid Mech. 209 (1989) 191226.

[14] R.L. Hoffman, A study of the advancing interface. I. Interface shape in liquid-gas systems, Journal of Colloid and Interface Science 50 (1975) 228235.

[15] M. Fermigier, P. Jenffer, An experimental investigation of the dynamic contact angle in liquid-liquid systems, J. Colloid. Interf. Sci. 146 (1991) 226-241.

[16] J. Eggers, H. A. Stone, Characteristic lengths at moving contact lines for a perfectly wetting fluid: the influence of speed on the dynamic contact angle, J. Fluid Mech. 505 (2004) 309-321.

[17] M. Renardy, Y. Renardy, J. Li, Numerical simulation of moving contact line problems using a volume-of-fluid method, J. Comput. Phys. 171 (2001) 243-263.

[18] P. D. M. Spelt, A level-set approach for simulations of flows with multiple moving contact lines with hysteresis, J. Comput. Phys. 207 (2005) 389-404.

[19] H. Ding, P. D. M. Spelt, Inertial effects in droplet spreading: a comparison between diffuse-interface and level-set simulations, J. Fluid Mech. 576 (2007), 287-296.

[20] S. Afkhami, S. Zaleski, M. Bussmann, A mesh-dependent model for applying dynamic contact angles to VOF simulations, J. Comput. Phys. 228 (2009) 5370-5389.

[21] Y. Sui, P. D. M. Spelt, Validation and modification of asymptotic analysis of rapid droplet spreading by numerical simulation, J. Fluid Mech., in press. Accessible online at http://hal.archives-ouvertes.fr/hal-00742532/

[22] M. Sussman, A. S. Almgren, J. B. Bell, P. Colella, L. H. Howell, M. L. Welcome, An adaptive level set approach for incompressible two-phase flows, J. Comput. Phys. 148 (1999) 81-124.

[23] S. Popinet, S. Zaleski, A front-tracking algorithm for accurate representation of surface tension, Int. J. Numer. Meth. Fluids 30 (1999) 775793.

[24] J.-B. Dupont, D. Legendre, Numerical simulation of static and sliding drop with contact angle hysteresis, J. Comput. Phys. 229 (2010) 2453-2478.

[25] F. Y. Kafka, E. B. Dussan V., On the interpretation of dynamic contact angles in capillaries, J. Fluid Mech. 95 (1979) 539-565.

[26] T. D. Blake, M. Bracke, Y. D. Shikhmurzaev, Experimental evidence of nonlocal hydrodynamic influence on the dynamic contact angle, Phys. Fluids 11 (1999) 1995-2007.

[27] T. D. Blake, J. M. Haynes, Kinetics of liquid/liquid displacements, J. Colloid Interface Sci. 30 (1969) 421-423.

[28] G. Russo, P. Smereka, A remark on computing distance functions, J. Comput. Phys. 163 (2000) 51-67.

[29] X. D. Liu, S. Osher, T. Chan, Weighted essentially non-oscillatory schemes, J. Comput. Phys. 115 (1994) 200-212.

[30] P. MacNeice, K. M. Olson, C. Mobarry, R. D. Fainchtein and C. Packer, PARAMESH: A parallel adaptive mesh refinement community toolkit, Comput. Phys. Commun. 126 (2000) 330354.

[31] W. Boender, A. K. Chesters, A. J. J. van der Zanden, An approximate analytical solution of the hydrodynamic problem associated with an advancing liquid-gas contact line, Intl. J. Multiphase Flow 17 (1991) 661-676.

[32] J. Lowndes, The numerical simulation of the steady movement of a fluid meniscus in a capillary tube, Journal of Fluid Mechanics 101 (1980) 631646.

[33] E. Ramé, On an approximate model for the shape of a liquid-air interface receding in a capillary tube, J. Fluid Mech. 342 (1997) 87-96.

[34] Y. Sui, P. D. M. Spelt, Sustained inertial-capillary oscillations and jet formation in displacement flow in a tube, Phys. Fluids 23 (2011) 122104.

[35] H. Ding, E. Q. Li, F. H. Zhang, Y. Sui, P. D. M. Spelt, S. T. Thoroddsen, Propagation of capillary waves and ejection of small droplets in rapid drop spreading, J. Fluid Mech. 697 (2012) 92-114.

[36] P. Sheng, M. Zhou, Immiscible-fluid displacement: contact-line dynamics and the velocity-dependent capillary pressure, Phys. Rev. A 45 (1992) 5694–5708.